TRAUMATIC BRAIN INJURY

Preclinical characterization of macrophage-adhering gadolinium micropatches for MRI contrast after traumatic brain injury in pigs

Lily Li-Wen Wang[1,2,3], Yongsheng Gao[1,2], Vineeth Chandran Suja[1,2], Masen L. Boucher[4], Suyog Shaha[1,2], Neha Kapate[1,2,3], Rick Liao[1,2], Tao Sun[1]†, Ninad Kumbhojkar[1,2], Supriya Prakash[1,2], John R. Clegg[1,2]‡, Kaitlyn Warren[4], Morgan Janes[1,2,3], Kyung Soo Park[1,2], Michael Dunne[1,2], Bolu Ilelaboye[1], Andrew Lu[1], Solomina Darko[1], Camilo Jaimes[5], Rebekah Mannix[4,6], Samir Mitragotri[1,2]*

The choroid plexus (ChP) of the brain plays a central role in orchestrating the recruitment of peripheral leukocytes into the central nervous system (CNS) through the blood-cerebrospinal fluid (BCSF) barrier in pathological conditions, thus offering a unique niche to diagnose CNS disorders. We explored whether magnetic resonance imaging of the ChP could be optimized for mild traumatic brain injury (mTBI). mTBI induces subtle, yet influential, changes in the brain and is currently severely underdiagnosed. We hypothesized that mTBI induces sufficient alterations in the ChP to cause infiltration of circulating leukocytes through the BCSF barrier and developed macrophage-adhering gadolinium [Gd(III)]–loaded anisotropic micropatches (GLAMs), specifically designed to image infiltrating immune cells. GLAMs are hydrogel-based discoidal microparticles that adhere to macrophages without phagocytosis. We present a fabrication process to prepare GLAMs at scale and demonstrate their loading with Gd(III) at high relaxivities, a key indicator of their effectiveness in enhancing image contrast and clarity in medical imaging. In vitro experiments with primary murine and porcine macrophages demonstrated that GLAMs adhere to macrophages also under shear stress and did not affect macrophage viability or functions. Studies in a porcine mTBI model confirmed that intravenously administered macrophage-adhering GLAMs provide a differential signal in the ChP and lateral ventricles at Gd(III) doses 500- to 1000-fold lower than those used in the current clinical standard Gadavist. Under the same mTBI conditions, Gadavist did not offer a differential signal at clinically used doses. Our results suggest that macrophage-adhering GLAMs could facilitate mTBI diagnosis.

INTRODUCTION

The choroid plexus (ChP), the primary source of cerebrospinal fluid (CSF) in the brain, is a highly vascularized structure lined by a specialized epithelial layer called ependyma, serving as the blood-CSF (BCSF) barrier (*1*). The ChP has only recently gained attention for its role as the gatekeeper of the infiltration of peripheral immune cells into the CSF (*2*). The ChP orchestrates the recruitment of leukocytes into the central nervous system (CNS) during multiple pathologies by increasing the expression of adhesion molecules and enhancing the secretion of chemokines and cytokines, thus making it a key player in numerous CNS disorders (*3*, *4*). Accordingly, although still understudied in clinical neuroimaging, there has been growing interest in imaging the morphological and functional changes in the ChP for diagnostic and prognostic evaluation of various neuroinflammatory disorders (*5*). Because of its high sensitivity to physical forces, the ChP is postulated to play a key role in the pathology of traumatic brain injury (TBI) (*6*). In particular, brain injuries are known to induce the disruption of the BCSF barrier at the ChP followed by leukocyte infiltration (*7*). We hypothesized that this unique attribute of the ChP can be exploited to facilitate the clinical diagnosis of TBI.

TBI is a global challenge that represents one of the leading causes of death and disability, with an estimated 69 million individuals affected worldwide each year (*8*). TBI can be categorized into mild, moderate, and severe, with mild TBI (mTBI) accounting for about 70 to 90% of the reported cases (*9*). Although mTBI is characterized by transient neurophysiological alterations, the long-term effects of mTBI can persist for months to years (*10*). mTBI is also associated with an increased risk of neuropsychiatric and neurodegenerative diseases, such as depression, dementia, and Parkinson's disease (*11*–*13*). Despite the disease burden of mTBI, as many as 60 to 90% of mTBI cases go undiagnosed even after a clinical investigation (*14*). Objective markers of injury, such as neuroimaging, are needed to improve diagnosis. For this reason, magnetic resonance imaging (MRI) is sometimes used to evaluate patients with suspected TBI (*15*). However, the diagnostic utility of MRI in mTBI has not been established. Specifically, conventional MRI sequences have neither demonstrated adequate performance to justify the routine use in mTBI nor offered important insights into the underlying pathophysiology of mild injury.

MRI contrast agents may increase the diagnostic utility of routine clinical MRI, as well as offer insights into mTBI pathophysiology, in part through the detection of mTBI-induced changes in the BCSF

[1]John A. Paulson School of Engineering and Applied Sciences, Harvard University, Allston, MA 02134, USA. [2]Wyss Institute for Biologically Inspired Engineering, Boston, MA 20115, USA. [3]Harvard-MIT Division of Health Sciences and Technology, Massachusetts Institute of Technology, Cambridge, MA 02139, USA. [4]Division of Emergency Medicine, Boston Children's Hospital, Boston, MA 02115, USA. [5]Department of Radiology, Boston Children's Hospital, Boston, MA 02115, USA. [6]Departments of Pediatrics and Emergency Medicine, Harvard Medical School, Boston, MA 02115, USA.
*Corresponding author. Email: mitragotri@seas.harvard.edu
†Present address: Department of Bioengineering, Northeastern University, Boston, MA 02115, USA.
‡Present address: Stephenson School of Biomedical Engineering, University of Oklahoma, Norman, OK 73019, USA.

barrier (*16*, *17*). Gadolinium [Gd(III)]–based contrast agents (GBCAs) are the standard choice for clinical MRI because of their strong paramagnetic properties, effective relaxation enhancement, excellent in vivo stability, and efficient clearance in patients without kidney diseases (*18*). In addition, efforts have been made to develop next-generation GBCAs with enhanced relaxivity (*19*), a parameter that describes the contrast agent's ability to modify nearby proton relaxation times, thereby directly influencing image contrast and serving as an indicator of its effectiveness in medical imaging contrast enhancement (*20*). However, it is not known whether GBCAs can specifically detect changes in the ChP after mTBI. This is especially relevant to the pathophysiology of mTBI where circulating immune cells are likely to cross the perturbed BCSF barrier. Thus, we hypothesized that the imaging of immune cell infiltration into the ChP can potentially offer a new sensitive imaging modality to diagnose mTBI and provide insights into the pathophysiology of mTBI.

Here, we report a contrast agent that is specifically designed to leverage macrophage infiltration across the BCSF barrier. Macrophages were chosen owing to their superior inflammation-homing ability, which is driven by the chemotactic gradient and their key role in brain infiltration (*21*, *22*). Specifically, we report Gd(III)-loaded anisotropic micropatches (GLAMs) that adhere to macrophages for improved mTBI diagnosis. GLAMs are hyaluronic acid–based discoidal microparticles, which bind to macrophages but resist phagocytosis because of their anisotropic morphology, enabling stable loading of Gd(III) onto the cell surface. GLAMs can be fabricated at scale and can incorporate Gd(III) with greater relaxivities than commercial GBCAs. Macrophage-hitchhiking GLAMs (M-GLAMs) were prepared by ex vivo incubation of GLAMs with macrophages. Studies in a porcine mTBI model confirmed that M-GLAMs provide a differential signal in the regions of interest [ROIs; the ChP and lateral ventricles (LVs)] of sham and mTBI pigs at Gd(III) doses 500- to 1000-fold lower than those used in the current clinical standard Gadavist (fig. S1). Under the same mTBI conditions, Gadavist did not offer a differential signal even at clinically used doses.

RESULTS

Design and fabrication of GLAMs

T1 MRI signals arising from the GBCA necessitates water proton-Gd(III) interactions. Hence, a hydrogel-based material was chosen to prepare GLAMs. Hyaluronic acid was selected as the material because of its biocompatibility and interactions with cells by CD44 (*23*). To achieve stable loading of Gd(III) into the hydrogel, a Gd(III) methacrylic acid [$Gd(MAA)_3$] precursor was synthesized and reacted with Alexa Flour 555–labeled methacrylated hyaluronic acid (HAMA) and poly(ethylene glycol) dimethacrylate (PEGDMA) using the photoinitiated free radical polymerization reaction (Fig. 1A and fig. S2; see Supplementary Materials and Methods for detailed synthesis and characterization). The fabrication method of Gd(III)-loaded hydrogels was first validated as a bulk material. A series of rheological tests, including oscillatory time-sweep, amplitude-sweep, and frequency-sweep experiments, was conducted to measure the storage modulus (G′) and loss modulus (G″) of hydrogels, two parameters that describe mechanical properties and behavior of a hydrogel under different conditions. These studies confirmed the formation of hydrogels (Fig. 1B and fig. S3). The onset of gelation occurred at 7 s after ultraviolet (UV) exposure when G′ became equal to G″ (Fig. 1B, i) (*24*). The storage modulus G′ plateaued after 2 min of UV exposure, suggesting the completion of cross-linking. The frequency-sweep test further showed frequency-independent G′ and G″, as well as an averaged storage modulus of 10.25 ± 0.58 kPa (Fig. 1B, ii), confirming the formation of a stable and covalently cross-linked hydrogel network (*25*).

Next, we aimed to transfer the bulk Gd(III) hydrogel chemistry to the microscale for GLAM fabrication. Specifically, the discoidal structure of GLAM is a key feature because disc-shaped particles have been demonstrated to adhere to macrophages without internalization (*26*). However, preparing anisotropic micrometer-sized hydrogel disks with dimensions smaller than the cell is a challenging task. Although techniques, such as particle replication in nonwetting templates (PRINTs) (*27*) and discontinuous dewetting in a degassed mold (*28*), have been developed to fabricate anisotropic subcell-sized hydrogel microparticles at scale, neither of them has been used for biopolymers with high molecular weight and viscosity (*29*, *30*). Hence, we engineered a new methodology to fabricate GLAMs.

A polydimethylsiloxane (PDMS) template was first prepared using soft lithography (fig. S4) (*31*), which was then used to form GLAMs using imprint lithography (*32*) and reactive ion etching (Fig. 1C) (*33*). Plasma-treated PDMS templates with an 8-μm hole array were spin-coated with Gd(III) hydrogel precursors and cross-linked by UV exposure. Plasma treatment was used to increase the surface energy of the PDMS template, leading to greater hydrophilicity to enable hydrogel deposition (*34*). An interconnecting hydrogel film was inherently formed during spin-coating because of the high surface energy of PDMS (*35*), preventing the formation of individual GLAMs (Fig. 1D, i). Therefore, inductively coupled plasma-reactive ion etching by oxygen was applied to remove this embossed film. GLAMs were then printed on a poly(vinyl alcohol) (PVA)–coated surface. High efficiency of the printing process was achieved by overnight freezing of the PDMS template post-etching at −80°C. This freezing step led to a 16-fold improvement in the efficiency of printing (fig. S5), likely because of the differential thermal expansion coefficients of PDMS and hydrogel, which enhanced the separation of GLAMs from the template (*36*). Printed GLAMs were collected in PBS and purified through centrifugation. The final collected GLAMs were imaged by fluorescence microscopy, showing a suspension of GLAMs with a discoidal shape (Fig. 1D, ii). Loading and stability of Gd(III) in GLAMs were quantified using inductively coupled plasma mass spectrometry (ICP-MS). Negligible (<0.7%) free Gd(III) was released and detected in cell culture medium, thus confirming the covalent incorporation of Gd(III) in GLAMs. Moreover, the loading remained stable for at least 2 weeks (Fig. 1E). Long-term storage of GLAMs under frozen conditions (>1 month) did not adversely affect the loading (fig. S6).

Contrast efficacy of $Gd(MAA)_3$ and GLAMs

Relaxivities of $Gd(MAA)_3$ and GLAMs were assessed using a 7-T MRI scanner with a longitudinal T1 mapping sequence. A clinical standard MRI contrast agent, Gadavist, was used as a comparator (Fig. 2A). Both Gadavist and free $Gd(MAA)_3$, the precursor of GLAM, demonstrated a Gd(III) concentration–dependent T1 contrast (Fig. 2B). A concentration-dependent quenching effect was seen for Gadavist and $Gd(MAA)_3$, where the T1 signal peaked and decreased with further increase in Gd(III) concentration, a phenomenon arising likely from the dominance of the T2 effects at a high Gd(III) concentration (*37*, *38*). Before the saturation threshold, the relaxivity of $Gd(MAA)_3$ (9.95 ± 0.03 mM^{-1} s^{-1}) was markedly

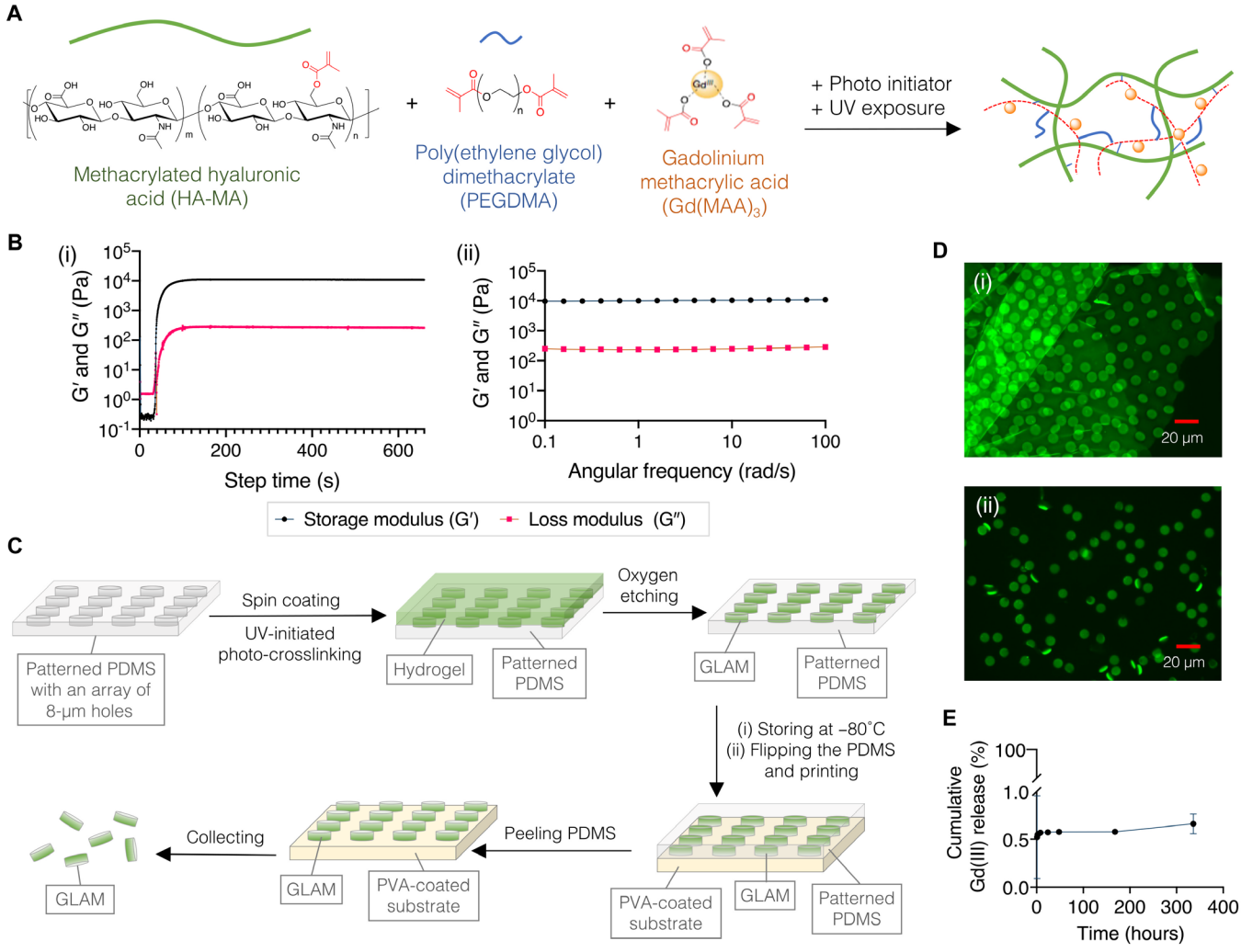

Fig. 1. Design and characterization of GLAMs. (**A**) The primary components of GLAMs include HAMA, PEGDMA, and Gd(MAA)$_3$. A hydrogel network is formed by photopolymerization upon the addition of I2959 photoinitiator and exposure of the ultraviolet (UV) light. (**B**) Dynamic oscillatory rheological characterization of the hydrogel with time sweeps (i) and frequency sweeps (ii). Storage modulus (G′) and loss modulus (G″) were recorded in each test. The UV light was then applied at 30 s. At 7 s after UV exposure, the gelation starts as G′ = G″, corresponding to the gel point of the hydrogel. In addition, G′ reached the plateau of 10.82 ± 0.61 kPa at ~2 min (n = 3). (**C**) Schematic illustration of GLAM fabrication process, including hydrogel deposition by spin coating, oxygen etching, freezing, printing and peeling, and collecting. (**D**) Fluorescence microscopy images of GLAMs without (i) and with the oxygen etching step (ii) in PBS. (**E**) Cumulative release of Gd(III) from GLAMs over 14 days in cell culture media, shaking at 150 rpm at 37°C (n = 3).

higher than that of Gadavist (3.63 ± 0.01 mM^{-1} s^{-1}; Fig. 2C and fig. S7), demonstrating the potential of Gd(MAA)$_3$ in itself as an effective T1 contrast agent.

GLAMs also exhibited a concentration-dependent relaxivity (Fig. 2D). The relaxivity per Gd(III) encapsulated in GLAMs increased when the payload increased from low Gd(MAA)$_3$ loading to medium loading (25.14 ± 4.65 to 34.69 ± 0.31 mM^{-1} s^{-1}), whereas it dropped in the case of high Gd(MAA)$_3$ loading (26.09 ± 0.82 mM^{-1} s^{-1}). Still, the relaxivity per Gd(III) was 8- to 11-fold higher in GLAM compared with that in Gadavist (Fig. 2E and fig. S7). High relaxivity of Gd(III) in the particulate form compared with the free form has been previously reported in the literature (*39*). The enhancement of relaxivity of Gd(III) in GLAMs compared with Gadavist can be attributed to the reduced mobility of Gd(III) in the hydrogel, thus reducing the orientational freedom within the particle and the increase in the rotational correlation time (*40*). Relaxivity per GLAM particle, calculated by multiplying the amount of Gd(III) ions per GLAM with the relaxivity per Gd(III), exhibited a monotonic correlation with Gd(MAA)$_3$ loading (Fig. 2F). Therefore, GLAMs with high Gd(MAA)$_3$ loading were chosen for future studies.

M-GLAM preparation and characterization

The adhesion of GLAMs to macrophages was examined by fluorescence microscopy and flow cytometry using both murine and porcine macrophages. GLAMs exhibited high adhesion to macrophages (M-GLAMs), as confirmed by fluorescence microscopy (Fig. 3A). The efficiency of GLAM adhesion to murine macrophages, measured using flow cytometry, increased as GLAM:macrophage ratio rose. Specifically, as the GLAM:macrophage ratio increased from 1.5:1 to 3:1, the adhesion efficiency increased from 51 to 72% (Fig. 3B; see fig. S8 for the gating strategy). Comparable efficiencies were also seen in porcine macrophages, thus confirming that GLAM adhesion to macrophages

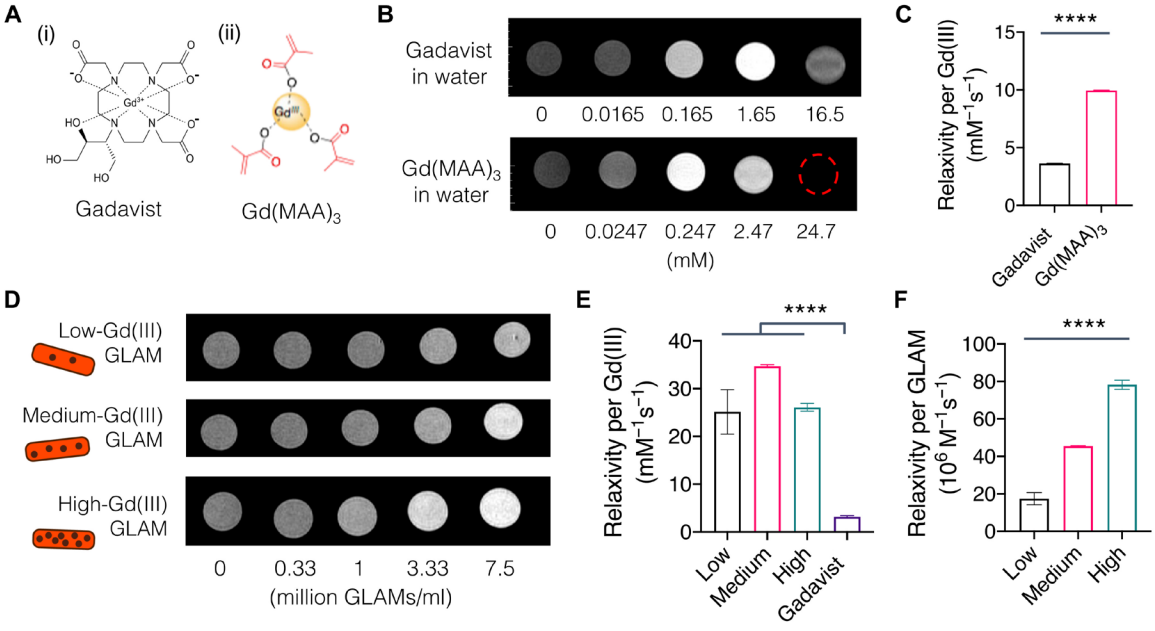

Fig. 2. Contrast efficacy of Gadavist, Gd(MAA)$_3$, and GLAMs. (**A**) Structure of small-molecule contrast agents: Gadavist and Gd(MAA)$_3$ (**B**) The T1-weight MR images of Gadavist and Gd(MAA)$_3$ dissolved in DI water at various concentrations, acquired at 7 T. (**C**) Relaxivity of Gadavist and Gd(MAA)$_3$ in DI water at 7 T. (**D**) The T1-weight MR images of GLAMs suspended in the Matrigel at various particle concentrations, acquired at 7 T. GLAMs were loaded with different amounts of Gd(III) from low, medium, to high. (**E**) Relaxivity per Gd(III) in GLAMs and Gadavist in the Matrigel at 7 T. (**F**) Relaxivity per GLAM in the Matrigel at 7 T. For (E and F), the mean and SD of the relaxivity were obtained, respectively, from the slope and SE of a linear regression fit of T1 relaxation rate against Gd concentration as shown in fig. S7. For (C, E, and F), data were analyzed using unpaired *t* test; ****$P \leq 0.0001$.

was species independent (Fig. 3C). GLAMs remained adhered to macrophages under physiologically relevant shear stresses (0 to 20 Pa; Fig. 3D), showing the stability of M-GLAMs under disturbances. Previously frozen GLAMs exhibited slightly higher adhesion compared with freshly collected GLAMs (Fig. 3E), indicating that the freeze-thaw step did not adversely affect macrophage binding. To verify that binding of GLAMs is specific to phagocytic macrophages over other cell types, adhesion of GLAMs to primary porcine endothelial cells was examined. The adhesion efficiency of GLAMs to endothelial cells (6.2%) was significantly lower than that to macrophages (45.8%; $P \leq 0.0001$; fig. S9).

GLAMs did not induce toxicity to macrophages, as assessed by their viability (Fig. 3F). Macrophage viability remained at about 100% under all tested ratios. Expression of chemokine receptor CCR2, which is critical for immune cell trafficking to the lesions of TBI (*41*), was not affected by GLAM adhesion (Fig. 3G). The transmigration capability of macrophages was retained after adhesion of GLAMs, as evaluated by a transwell migration assay (Fig. 3H). In addition, a significant increase in the number of migrated M-GLAMs through the transwell membrane in response to chemoattractant CCL2 indicated the maintenance of chemotactic ability of macrophages after GLAM binding ($P \leq 0.01$).

Biodistribution and tolerability of M-GLAMs in the murine model

In vivo delivery of GLAMs and M-GLAMs was first assessed in healthy BALB/c mice with a particular focus on tolerance and biodistribution and comparison to Gadavist. Accumulation of GBCAs in the kidney is known to elevate the risk of nephrogenic systemic fibrosis in patients with existing renal diseases and is contraindicated in these patients (*42*); thus, it is important to evaluate the kidney accumulation of Gd(III) upon contrast administration. The mouse model was chosen for the biodistribution study because of the similarity of murine organs (for example, shape, structure, and physiology) and circulatory system to those of humans (*43*). Because the structure and composition of human and mouse brains are remarkably different (*44*), the mouse study aimed to assess tolerance and biodistribution in healthy mice.

Injections of Gadavist, GLAMs, and M-GLAMs were well tolerated by healthy BALB/c mice. Gadavist exhibited substantial renal accumulation in mice at 15 min after injection [Fig. 4A (i) and fig. S10A]. Gadavist accumulation was assessed at the early time point of 15 min, aligning with the rapid clearance of GBCAs and its clinical relevance. GLAMs, on the other hand, were mainly distributed in the lung, followed by liver and spleen, with barely any accumulation in the kidney [Fig. 4A (ii) and fig. S10B]. M-GLAMs exhibited a similar Gd(III) accumulation pattern as the GLAMs alone [Fig. 4A (iii) and fig. S10C]. Negligible renal accumulation of GLAMs and M-GLAMs revealed that the Gd(III) was stably conjugated in the particles without leakage. Only about 8, 0.3, and 0.0027% of total injected dose of Gadavist was detected in all the collected organs at 15 min, 1 hour, and 24 hours after injection, respectively (fig. S10D), suggesting that Gadavist was rapidly cleared and almost completely excreted from the body within 24 hours. In contrast, GLAMs and M-GLAMs demonstrated stable retention in the vital organs (~80%) over a period of 24 hours, showing the potential feasibility of using M-GLAMs for long-term disease monitoring or delayed imaging. Although M-GLAMs remained in the body for an extended time, the delivered Gd(III) dose from M-GLAMs was ~580 times lower than that from Gadavist (2000 nmol per mouse for Gadavist and 3.4 nmol per mouse for M-GLAMs), thus keeping the body's exposure to Gd(III) at a very low amount.

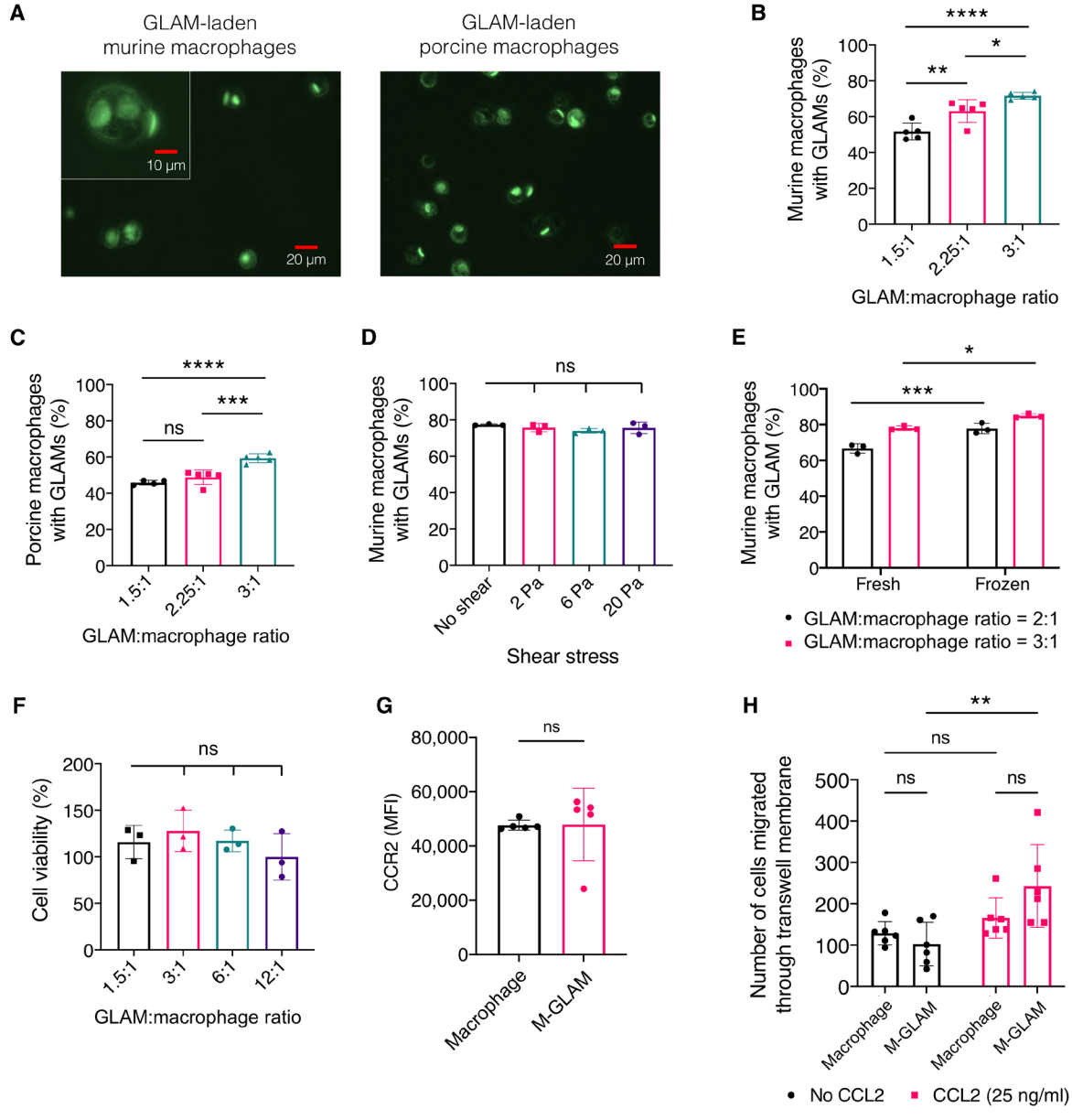

Fig. 3. In vitro characterization of the M-GLAMs and the effect of GLAMs on macrophage functions. (**A**) Fluorescence microscopy images of GLAM-laden murine (left) or porcine macrophages (right). Association of the GLAMs with primary murine (**B**) and porcine macrophages (**C**) at various GLAM-to-macrophage ratios ($n \geq 4$). (**D**) Effect of shear stress on adhesion efficiency ($n = 3$). (**E**) Effect of freeze-thaw process on adhesion efficiency ($n = 3$). Freshly prepared GLAMs (fresh) or GLAMs that underwent freeze-thaw process (frozen) were tested. (**F**) Effect of GLAMs on macrophage viability after 24 hours by MTS assays at various GLAM:macrophage ratios ($n = 3$). (**G**) Effect of GLAMs on chemokine receptor CCR2 expression ($n = 5$). (**H**) Effect of GLAMs on macrophage migration after 2 hours ($n = 6$). Migration was assessed using a transwell assay, where macrophages or M-GLAMs were seeded on 5-μm inserts, and medium containing no CCL2 or CCL2 at 25 ng/ml was added to the receiver well. For (B to D and F), data were analyzed by one-way ANOVA with Tukey's post hoc test. For (E and H), data were analyzed by two-way ANOVA with Tukey's post hoc test. For (G), data were analyzed using unpaired *t* test; ns, not significant; $^{*}P \leq 0.05$, $^{**}P \leq 0.01$, $^{***}P \leq 0.001$, and $^{****}P \leq 0.0001$.

Long-term systematic toxicity of M-GLAMs was evaluated in healthy C57BL/6 mice by histology and serum chemistry panel test 7, 14, and 28 days after injection. No marked abnormalities were seen in vital organs of M-GLAM–injected mice (Fig. 4B). The serum concentration of aspartate transaminase and alanine transaminase, biomarkers that typically elevate in response to liver damage (*45*), remained unchanged or slightly lower in M-GLAM–injected animals compared to the saline group (Fig. 4C). The creatinine and blood urea nitrogen, markers that typically elevate upon kidney dysfunction (*46*), did not show any marked increase in M-GLAM–injected animals compared to the saline control. The M-GLAM–injected mice showed no statistically significant differences in other common biochemical markers, such as globulin and creatine kinase, compared to the saline mice ($P > 0.05$).

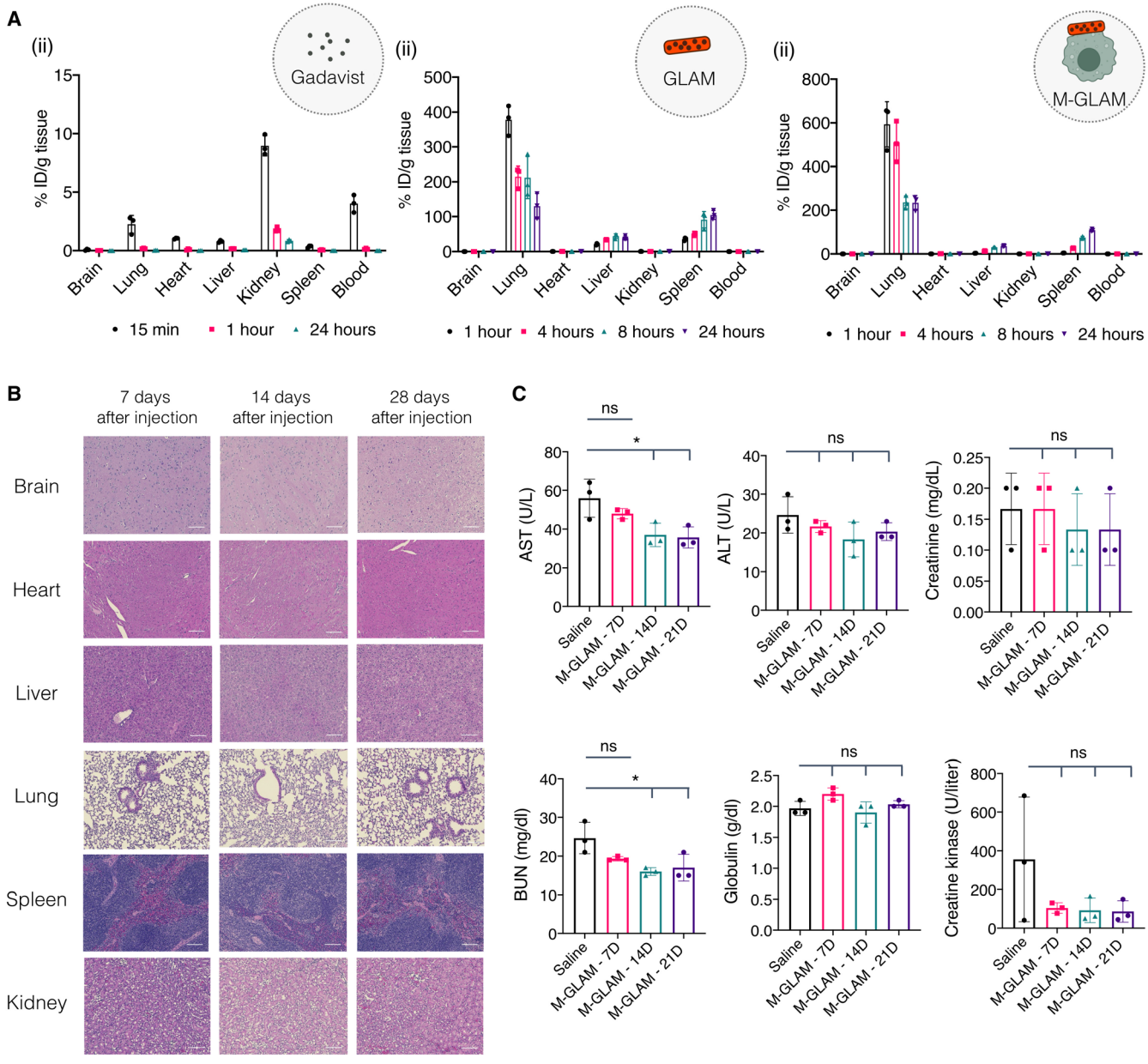

Fig. 4. In vivo biodistribution study and long-term toxicity evaluation in healthy mice. (**A**) Mice were injected with Gadavist (i), GLAMs (ii), and M-GLAMs (iii). For the Gadavist group, mice were euthanized at 15 min, 1 hour, and 24 hours after injection ($n = 3$), whereas the GLAM and M-GLAM groups were euthanized at 1, 4, 8, and 24 hours after injection ($n = 3$). After euthanasia, the organs were immediately collected and processed to quantify the Gd(III) amount in each organ by ICP-MS. Data are presented in percent of injected dose per gram of tissue (%ID/g), with percent of injected dose (%ID) data shown in fig. S10. (**B**) Representative images of hematoxylin and eosin staining of mouse vital organs 7, 14, and 28 days after M-GLAM injection. Organs were collected at 7, 14, and 28 days after M-GLAM injection. Scale bars, 100 μm. (**C**) Serum biomarker concentrations, including aspartate aminotransferase (AST), alanine aminotransferase (ALT), creatinine, blood urea nitrogen (BUN), globulin, and creatinine kinase ($n = 3$). Mice were injected with saline or M-GLAMs, and the serum samples were collected at 7, 14, and 28 days after M-GLAM injection. For (C), data were analyzed by one-way ANOVA with Tukey's post hoc test; $^*P \leq 0.05$.

Evaluation of M-GLAMs for mTBI diagnosis in the porcine model

The utility of M-GLAMs in diagnosing mTBI was assessed in a porcine model. The model was chosen because of the compositional, structural, anatomical, and biomechanical similarity between porcine and human brains (*47*). To ensure maximum clinical relevance in the current study, we opted for a single-dose regimen and selected the 2-day time point (time period from injury to MRI), considering that the vast majority of TBI patients evaluated in acute care hospitals present within 48 hours of injury. Gadavist and M-GLAMs were administered in sham and mTBI pigs, and high-resolution T1 maps were acquired by a 3-T MRI scanner before and after contrast agent injection (that is, prescans and post-scans, respectively). Gadavist (0.1 mmol/kg; ~2.2 to 2.8 mmol per animal) or M-GLAMs (~75 million to 175 million

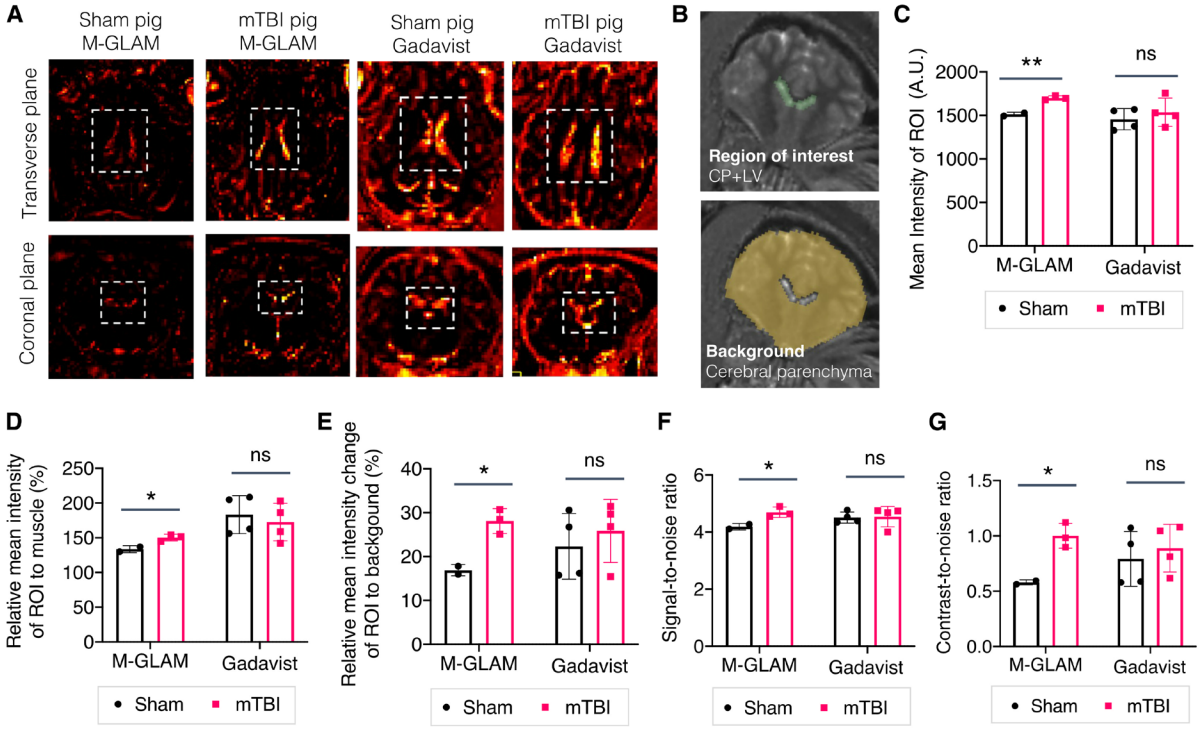

Fig. 5. MRI studies for mTBI diagnosis in the porcine model. (**A**) Representative subtracted T1 relaxivity maps of the pigs injected with M-GLAMs and Gadavist. T1 maps were acquired before (prescans) and after the administration of imaging agents (post-scans). Subtracted images were then obtained by registering both scans by ITK-SNAP (an interactive software for segmenting anatomical structures in medical images), followed by subtracting post-scans with prescans by convert3D of ITK-SNAP. The dotted squares highlight the location of the lateral ventricle (LV) and ChP, which was the region of interest (ROI). (**B**) Representative post-scans of MRI-generated T1 maps highlighting the ROI (top) and background (bottom) by ORS Dragonfly. (**C**) Quantitative analysis of MR signal intensities in the ROI of sham pigs injected with M-GLAMs ($n = 2$) or Gadavist ($n = 4$) and mTBI pigs injected with M-GLAMs ($n = 3$) or Gadavist ($n = 4$) by the mean pixel intensity ($\bar{I}_{ROI}$). Post-scans were used. (**D**) Relative mean intensity of ROI to muscle based on the post-scans, obtained by $\bar{I}_{ROI} / \bar{I}_{muscle}$. (**E**) Relative mean intensity changes of ROI to cerebral background based on the post-scans, calculated by $(\bar{I}_{ROI} - \bar{I}_{background}) / \bar{I}_{background}$. (**F**) Signal-to-noise ratio (SNR) of the post-scans was calculated by $\bar{I}_{ROI} / \Delta_{background}$. (**G**) Contrast-to-noise ratio (CNR) of the post-scans was acquired by $(\bar{I}_{ROI} - \bar{I}_{background}) / \Delta_{background}$. Δ, SD. For (C to G), data were analyzed using unpaired *t* test; $^*P \leq 0.05$ and $^{**}P \leq 0.01$. A.U., arbitrary units.

per animal) were delivered intravenously. To serve as a clinical comparator, the Gadavist dose was matched to a typical clinical recommendation. M-GLAM dose was selected to keep the dose of injected macrophages comparable to previously reported values for adoptive macrophage therapies in the clinic (*48*). Mild facial edema and/or hives were observed on the injection side of the pig in three of five pigs administered with M-GLAMs. Red rash was shown in one of eight pigs administered with Gadavist. However, all symptoms and changes were transient and self-resolved during the recovery time of the pigs from anesthesia.

To assess the potential of the ChP as an ROI for mTBI, images were analyzed on the basis of subtracted T1 relaxivity maps (namely, post-scans subtracted by prescans) using ITK-SNAP (see the Supplementary Materials for the detailed method of MRI data analysis) (*49*). Gadavist, as a small molecule, distributed throughout the microvascular extra-axial structures (for example, arteries, veins, and dural sinuses) and the ChP, clearly delineating their anatomy (Fig. 5A); expectedly, no parenchymal accumulation of Gadavist was noted. Furthermore, no discernable differences were noted between the sham and mTBI pigs. Subtracted T1 maps of the pigs with M-GLAM injection were overall dimmer compared to those with Gadavist administration, at least in part because the Gd(III) dose in M-GLAMs was 500- to 1000-fold lower than that in the case of Gadavist. However, a notable difference in signal intensity was observed in the ChP and LV between sham and mTBI pigs in the case of M-GLAMs (Fig. 5A, dashed rectangles).

To assess the ability of the ChP to serve as a clinically usable ROI for mTBI, in the absence of pretrauma scans, as often is the case clinically, only post-scans were used to define the MRI signals in the ROI and its surrounding cerebral background by extracting the pixels of both areas by ORS Dragonfly (Fig. 5B). The mean intensity in the ROI ($\bar{I}_{ROI}$) was significantly different between the sham and mTBI pigs administered with M-GLAMs ($P \leq 0.01$), whereas no difference was seen in case of Gadavist ($P > 0.05$; Fig. 5C). Furthermore, given that MRI automatically adjusts to prevent the saturation of the signals, we aimed to mitigate this bias through normalizing $\bar{I}_{ROI}$ by the average muscle mean intensity ($\bar{I}_{muscle}$). Normalized intensity ($\bar{I}_{ROI} / \bar{I}_{muscle}$) exhibited a significant difference in sham and mTBI pig brains for the M-GLAM group ($P \leq 0.05$), but not for the Gadavist group ($P > 0.05$; Fig. 5D).

Enhancement of the mean ROI intensity ($\bar{I}_{ROI}$) compared with that in the surrounding background tissue (cerebral parenchyma, $\bar{I}_{background}$) offers another means to assess mTBI. In the M-GLAM group, the normalized intensity ($[\bar{I}_{ROI} - \bar{I}_{background}] / \bar{I}_{background}$) increased from 16.9% in sham pigs to 28.08% in mTBI pigs ($P < 0.05$; Fig. 5E). In

contrast, no difference was observed in the sham and mTBI pigs when injected with Gadavist (22.33% in sham versus 25.85% in mTBI, $P = 0.6$). The signal-to-noise ratio (SNR; $\bar{I}_{ROI} / \Delta_{background}$), contrast-to-noise ratio [CNR; $(\bar{I}_{ROI} - \bar{I}_{background}) / \Delta_{background}$], and the coefficient of variation for ROI and background (CoV; $\Delta_{ROI} / \bar{I}_{ROI}$ and $\Delta_{background} / \bar{I}_{background}$) were also obtained (Fig. 5, F and G, and fig. S11), where Δ is the SD of the signal. Both SNR and CNR were significantly different between sham and mTBI pigs only in the case of M-GLAMs ($P \leq 0.05$), but not in the case of Gadavist, with a particularly notable difference observed in the case of CNR ($P > 0.05$; Fig. 5G). A lower CoV of ROI in the M-GLAM groups over Gadavist implies that M-GLAMs provide a more uniform enhancement of MRI signal in the ROI (fig. S11).

Tolerance of M-GLAMs and Gadavist was assessed by histopathology (fig. S12). Vital organs were harvested, fixed, sectioned, and stained with hematoxylin and eosin for histological analysis at 4 days after injection. No conspicuous histological abnormality was seen in the organs of either Gadavist or M-GLAM–injected animals, as assessed by an independent board-certified veterinary pathologist. Some mild changes, observed in the livers, lungs, and kidneys of both groups, were attributed to the euthanasia and fixation procedures. Neuroinflammation after mTBI was also confirmed by histopathology by staining ionized calcium binding adaptor molecule 1 ($IBA1^+$) macrophages within coronal whole porcine brain slices that included the ROI (ChP and LV). Analyses revealed increased macrophage density within the brain tissues of the mTBI animals compared with the sham groups (fig. S13).

DISCUSSION

M-GLAMs provide a means of leveraging immune cells to monitor brain inflammation after mTBI. GLAMs were prepared using a fabrication process to build hydrogels into discoidal microparticles. The results presented here demonstrate that Gd(III) can be incorporated into GLAMs with at least an eightfold enhancement in relaxivity. GLAMs were stable during the freeze-thaw process, which is critical in improving the particle yield and essential for long-term storage. GLAMs are made of materials (that is, hyaluronic acid and polyethylene glycol) that have been widely used in Food and Drug Administration–approved products (*50*, *51*).

M-GLAMs were prepared by incubating GLAMs with allogeneic macrophages. Adhesion of GLAMs does not adversely affect macrophage functions, including cell viability, migration, and surface receptor expression. Stable binding of GLAMs to the macrophage surface can result from the balance between the factors that promote and impede phagocytosis. Macrophages are highly effective in binding, engulfing, and eliminating particulates with dimensions larger than 0.5 μm (*52*). They are capable of proficiently internalizing even unopsonized particles by scavenger receptor-mediated phagocytosis through the zipper mechanism (*53*, *54*). In addition to the size, the shape of the particle largely affects the phagocytosis process; specifically, particles with a high aspect ratio can evade phagocytosis by preventing the formation of the actin structures required for particle ingestion (*55*). The balance of these two opposite facets provides the optimal niche for GLAMs to attach to the macrophage surface with prolonged retention times. This feature enables the stable loading of Gd(III) on the cell surface through preventing degradation of Gd(III)-loaded particles by intracellular enzymes or acidic conditions and avoids the change of relaxivity of Gd(III) due to changes in pH (*56*). GLAMs are compatible with the carrier cells and can stably adhere to macrophages under different physiological shear stresses that they may encounter upon injection, circulation, extravasation, and migration (*57*). Together, the optimized manufacturing process, the biocompatibility of materials, and the stability of the system favor the clinical translation of this technology.

M-GLAMs provided a biodistribution profile that addresses current clinical challenges associated with GBCAs. Specifically, high concentrations of GBCAs are often needed for clinical diagnosis (*58*); thus, the use of GBCAs is contraindicated in patients with existing kidney dysfunctions because of the potential nephrotoxicity of Gd(III) and increased risk of nephrogenic systemic fibrosis in these patients (*59*). M-GLAMs were delivered at a dose 500- to 1000-fold lower compared with Gadavist. Furthermore, M-GLAMs exhibited negligible renal accumulation of Gd(III), thus altogether reducing renal exposure to Gd(III). The bulk structure of GLAMs is expected to be degraded in vivo by hyaluronidase (*60*), but the covalent bonds formed by the methacrylate groups are expected to be relatively stable (*61*, *62*). This can allow Gd(III) to be released from GLAMs in a macromolecular form, which has a higher stability and thus a lower tissue deposition and toxicity compared with small Gd(III) chelates (*63*, *64*). Furthermore, the long-term safety test revealed no evidence of systemic toxicity caused by M-GLAMs.

Diagnosis of mTBI remains a major challenge (*65*). Current clinical neuroimaging for TBI diagnosis usually focuses on finding observable structural damage, such as contusions, hematomas, or other injuries that disrupt the blood-brain barrier (BBB) in the brain parenchyma (*66*). However, to date, no imaging modality has demonstrated clinical utility in the management of TBI without structural brain injury (that is, mTBI). Although advanced MRIs reveal abnormalities in large group comparisons, the findings on arterial spin labeling, diffusion imaging, and MR spectroscopy lack biological and temporal specificity (*67*, *68*). Without pretrauma imaging and a history of mTBI, these advanced features cannot be reliably attributed to a traumatic injury and cannot differentiate a patient who is affected from one who is not. Hence, a remarkable advance in the field would be the identification of a dependable method to differentiate TBI from non-TBI using conventional imaging techniques to interrogate a single ROI such as the ChP. The results of the porcine studies presented here indicate that M-GLAMs could potentially differentiate healthy and injured brains by providing differential MRI signals in the region of the ChP and LV using the conventional MRI.

The differential homing of M-GLAMs in mTBI and sham pig brains can be attributed to the active trafficking ability of immune cells to the inflamed brain through the ChP, with the state of neuroinflammation being confirmed by detection of an increase in $IBA1^+$ macrophage density in postinjury brain tissues, and aligns with previously reported work in this porcine model (*69*). This mechanism is in line with the findings reported by others that myeloid cells traveled to the brain through the BCSF barrier after trauma (*70*). This migration is driven by the release of ChP-regulated chemokines and cytokines in synergy with adhesion molecules in the CNS (*71*). In addition, the high blood flow rate at the ChP (5- to 10-fold faster than that in other tissues) and fenestrated ChP capillaries provide an exceptional niche for circulating immune cells to access and interact with ChP stroma (*72*). These features may lead to the enhanced infiltration of M-GLAMs into the CSF through the BCSF barrier. Although the BBB

can potentially provide another route for immune cells to penetrate into the injured brain (*73*), we did not observe any overt change in BBB or nearby brain parenchyma in the MRI scans. This can potentially be attributed to the large surface of the BBB (5000-fold compared with the BCSF barrier) (*74*) that may hinder the localization of the contrast agents to achieve the critical concentration required for detectable MRI signals.

One primary limitation of this study is its small animal sample size, limiting the generalizability of the results. Furthermore, the observed results may not fully capture the diverse range of responses within the population. Future research involving larger cohorts is necessary to validate the identified trends and conclusions. Another constraint involves the potential migration of M-GLAMs to the inflamed brain in conditions other than mTBI by the ChP. Nonetheless, when used in conjunction with other elements of the clinical exam providing supplementary information, M-GLAM–based imaging holds the potential to enhance the diagnostic accuracy of mTBI.

Together, we demonstrated that M-GLAMs are a living contrast agent that enables us to image macrophage infiltration of the BCSF barrier and its vicinity (the ChP and LV) after mTBI. Future applications of M-GLAM might be expanded to other CNS disorders that involve the pathological changes at the ChP (*75*). In the studies presented here, allogenic macrophages were used to prepare M-GLAMs, and the clinical applications of M-GLAMs could potentially make use of engineered allogeneic macrophages that can be manufactured at scale. With further research focused on safety, manufacturing and evaluation of diagnostic performance in realistic clinical settings, M-GLAMs might expand current diagnostic tools for CNS disorders.

MATERIALS AND METHODS

Study design

Here, we aimed to design Gd(III) micropatches that adhere to macrophages to image macrophage infiltration through the ChP after TBI. We first characterized the physical properties of GLAMs and assessed their effects on macrophage viability and function in vitro.

To assess the in vivo biodistribution and tolerability of GLAM and M-GLAMs, each experimental group consisted of three mice. These mice received contrast agent injections, and subsequently, major organs and blood samples were collected. For biodistribution studies, Gd(III) levels in the tissues were quantified using ICP-MS. Tissue staining and blood chemistry panels were used for tolerability assessments. To evaluate the targeting capability of M-GLAMs toward inflamed brain tissue after mTBI in a porcine model, each experimental group comprised two to four pigs. These pigs were administered the contrast agent injections and underwent MRI imaging. Four days after the MRI scan, the animals were euthanized, and major organs were collected. Tissue staining was subsequently used to assess both tolerance and the extent of macrophage accumulation in the brain. Careful attention was given to controlling environmental variables, standardizing experimental procedures, and ensuring the consistency of measurements across all groups. In addition, the histological examination was conducted blinded to ensure unbiased assessment of the samples. The mouse experiments were conducted in accordance with protocols approved by Harvard University's Institutional Animal Care and Use Committee (protocol ID: 21-01-378). The swine experiments were conducted in accordance with protocols approved by Boston Children's Hospital Institutional Animal Care and Use Committee (protocol ID: 19-12-4110R*).

Hydrogel synthesis

The hydrogel was composed of an HAMA mixture (mass ratio of regular HAMA and fluorescent HAMA = 10:1; see the Supplementary Materials for synthesis and characterization), PEGDMA (1 k Da, obtained without purification from Polysciences), $Gd(MAA)_3$, and Irgacure 2959 photoinitiator (I2959; Sigma-Aldrich). To prepare the hydrogel mixture, $Gd(MAA)_3$ solution was first prepared in deionized (DI) water (1 wt%) with sonication. The regular HAMA and fluorescent HAMA were dissolved in $Gd(MAA)_3$ solution at the concentration of 3 wt% at room temperature (RT) overnight. Next day, I2959 was dissolved in Gd-MAA solution (2.5 wt%) at 60°C with stirring for at least 10 min, and PEGDMA solution was prepared in Gd-MAA solution (20 wt%) at 37°C. The final hydrogel solution was prepared by mixing the solutions of regular HAMA, fluorescent HAMA, I2959, PEGDMA, and $Gd(MAA)_3$ with a volume ratio of 10:1:4.2:1.7:1.

GLAM fabrication

Hydrogel solution was prepared by the aforementioned method. PDMS templates were prepared (see the Supplementary Materials for PDMS template preparation) and cut into 1 inch–by–1 inch quadrants. To increase the hydrophilicity of PDMS for hydrogel deposition, quadrants were then plasma-ashed with O_2 for 60 s (Thierry Corp.). Immediately after plasma treatment, quadrants were spin-coated with 200 μl of the hydrogel solution per quadrant at 4000 rpm for 90 s (at a ramp of 500 rpm/s), followed by UV exposure (365 nm; 50 W; Analytik Jena) for 10 min. The distance between the hydrogel and UV light source was critical for proper cross-linking. The residual hydrogel outside the cylindrical holes was then removed by oxygen plasma etching (80 mtorr and 100 W) at 20°C for 160 s by the load-locked high plasma density etcher (PlasmaPro 100 Cobra 300; Oxford Instruments). GLAMs were formed within the holes of PDMS templates. Next, the etched samples were placed in a −80°C freezer for better detachment of the GLAMs from the PDMS substrate.

GLAMs were retrieved from PDMS templates by printing modified from the work of Xia *et al.* (*76*). PVA-coated dishes, the printing substrate, were prepared by coating 2.5 ml of a 3% (w/v) PVA solution (13 to 23 kDa), followed by drying PVA in an oven at 65°C overnight. Before printing, the frozen samples were thawed at RT to prevent water condensation on the quadrant surface because the condensation can largely affect the printing yield. The coated side of a PVA dish was held ~2 cm over the beaker filled with DI water at 65°C for ~7 to 10 s. A GLAM-containing PDMS quadrant was instantly pressed onto the warmed PVA dish. To collect printed GLAMs, 3 ml of DI water or phosphate-buffered saline (PBS) was added to the dish with gentle washing, applied twice. The collected solution was filtered through a 20-μm cell strainer to remove any large debris, followed by centrifugation at 2000*g* for 2 min to obtain GLAMs. See the Supplementary Materials for the paramagnetic property characterization of GLAMs.

Preparation and characterization of M-GLAMs

Frozen GLAM solution was thawed to RT. GLAMs collected by centrifugation at 2000*g* for 2 min and were resuspended in culture media. Concurrently, bone marrow–derived macrophages (BMDMs) cultured in 24-well plates for 24 hours were transferred from the incubator, and the medium was slowly aspirated and replaced by fresh culture media. See the Supplementary Materials for murine and porcine BMDM culture. Then, GLAMs were counted and added to each well to achieve different GLAM:macrophage ratios (1.5:1, 2.25:1, and 3:1) with a final incubation volume of 0.5 ml per well. BMDMs were

then incubated with GLAMs at 37°C and 5% CO_2 for 1.5 hours without disturbance. After incubation, the supernatant containing unbounded GLAMs was aspirated, and the cells were washed by the addition of 0.5 ml of PBS and aspiration. To harvest M-GLAMs, 0.5 ml of Accumax was added to each well and incubated for 15 min at 37°C and 5% CO_2. The plate was removed from the cell culture incubator and gently thumped on the side several times. The solution was collected into 5-ml tubes with equal volume of culture media, followed by centrifugation at 300*g* for 5 min at 4°C. See the Supplementary Materials for the M-GLAM characterization.

Biodistribution of Gadavist, GLAMs, and M-GLAMs in mice

Healthy female BALB/c mice (RRID:IMSR_CRL:027) were intravenously administered with Gadavist (0.1 mmol/kg), GLAMs (10×10^6/ml in saline, 200 μl), or M-GLAMs (6×10^6/ml in saline, 200 μl). At certain time points after administration (15 min, 1 hour, and 24 hours for the Gadavist group; 1, 4, 8, and 24 hours for the GLAM and M-GLAM groups), submandibular blood was collected, and the mice were immediately euthanized. Next, the major organs (brain, lungs, heart, liver, spleen, and kidneys) were extracted, washed in PBS, and weighed. The organs were then transferred into 14-ml round bottom tubes, and radioimmunoprecipitation assay (RIPA) lysis buffer (EMD Millipore) was added to each organ (1 ml for brain, lung, heart, and kidney; 5 ml for liver; and 0.5 ml for spleen) before homogenization. In addition, 0.4 ml of RIPA was added to 0.1 ml of blood samples. The homogenized samples were mixed with concentrated aqua regia solution (HNO_3:HCl = 1:3; 0.5 ml for brain, lung, heart, and kidney; 2.5 ml for liver; 0.25 ml for spleen; and 0.1 ml for blood) for 2 days. The resulting solutions were then diluted by DI water (4.75 ml for brain, lung, heart, and kidney and 4 ml for spleen and blood) with no dilution for the liver sample, followed by centrifugation at 1200*g* for 5 min to obtain clear samples without tissue debris. Supernatants (4 ml) were slowly transferred to 15-ml conical tubes and subsequently mixed with 1 ml of internal standard solution [thulium (1 ng/ml) and indium in 2% (v/v) HNO_3; High-Purity Standards]. The mixture was then used for ICP-MS analysis, and the concentration was determined using a calibration curve made with Gd(III) ICP standard solution (High-Purity Standards).

MRI and contrast administration

Details of the porcine mTBI model can be found in the Supplementary Materials and Methods. Two MRI scans were performed on each animal: a preinjection scan (without contrast) and a postinjection scan (with contrast) at 2 days after injury. The animals were scanned using a 3-T scanner (Skyra; Siemens, Erlangen, Germany) located within the Radiology Department of Boston Children's Hospital. Within the sham and mTBI conditions, animals were randomly assigned to receive either the clinically available contrast agent Gadavist (1 mmol/ml, dose of 0.1 ml/kg, clinically used dose) (Bayer, Leverkusen, Germany) or M-GLAMs (~75 million to 175 million/10 ml of saline, 10 ml per pig; sham Gadavist, $n = 4$; sham M-GLAMs, $n = 2$; mTBI Gadavist, $n = 4$; mTBI M-GLAMs, $n = 3$). Swine were anesthetized with telazol (2.2 to 6.6 mg/kg), xylazine (1.1 to 2.2 mg/kg), and atropine (0.04 mg/kg), and vital signs (heart rate, respiratory rate, pulse oximetry, and core body temperature) were monitored throughout the procedure. Once induced, another blood draw was performed by superior vena cava. The animal was transported to the MRI facility and securely positioned on their back (supine) within the scanner with a 64-channel head and neck coil (Siemens, Erlangen, Germany). A magnetization-prepared 2 rapid acquisition gradient echo sequence was used with the following parameters: TR = 4000 ms, TI1/TI2 = 700, 2500 ms, α1/α2 = 4, 5°, BW = 230 Hz/pixel, 3× GRAPPA acceleration, and acquisition time = 9 min. Isotropic images (1 mm) were acquired with a field of view (FOV) of 43.6 cm by 20 cm. This sequence generates images with each of the individual inversion times and a T1 map with the same spatial resolution as the other sequences. In addition, two-dimensional fluid-inversion attenuation recovery (FLAIR) sequence was acquired in the coronal plane; the parameters for the sequence were as follows: TR = 9000 ms, TE = 108 ms, TI = 2500 ms, BW = 290, and FOV = 14 cm by 18 cm. FLAIR was used to evaluate the anatomy after injury and ensure that no unexpected contusions or hematomas occurred; these images were used only for expert neuroradiology review.

After the preinjection scans, the animal received the contrast agent. In the case of the animals receiving Gadavist, the animal began its postinjection scan ~5 min after injection, which is comparable to the time delay used clinically. In the case of the animals receiving the M-GLAMs, the animal received its postinjection scan 1 hour later, allowing the M-GLAMs to traffic into the brain. During this time, the animal's body temperature was maintained using Bair Hugger (3M, Maplewood, MN). The postcontrast injection scans were taken using the same parameters as described above. After the scans, the animal was returned to its cage to recover.

Statistical analysis

All statistical analyses were represented as means ± SE using GraphPad Prism 8 software. To determine statistical significance, unpaired Student's *t* test and one-way or two-way analysis of variance (ANOVA) with Tukey's post hoc test were used, as applicable. The replications of experiments are all biological replicates. Significance was determined at the following cutoff points (not significant, $P > 0.05$; $*P \leq 0.05$; $**P \leq 0.01$; $***P \leq 0.001$; and $****P \leq 0.0001$). Flow cytometry analyses were carried out using FCS Express 7. Raw data for all graphs in Figs. 1 to 5 are summarized in data file S1.

Supplementary Materials

This PDF file includes:

Materials and Methods
Figs. S1 to S13
References (*77*–*87*)

Other Supplementary Material for this manuscript includes the following:

Data file S1
MDAR Reproducibility Checklist

REFERENCES AND NOTES

1. K. Javed, V. Reddy, F. Lui, in *StatPearls [Internet]* (StatPearls Publishing, 2021).
2. J.-F. Ghersi-Egea, N. Strazielle, M. Catala, V. Silva-Vargas, F. Doetsch, B. Engelhardt, Molecular anatomy and functions of the choroidal blood-cerebrospinal fluid barrier in health and disease. *Acta Neuropathol.* **135**, 337–361 (2018).
3. A. C. Yang, F. Kern, P. M. Losada, M. R. Agam, C. A. Maat, G. P. Schmartz, T. Fehlmann, J. A. Stein, N. Schaum, D. P. Lee, K. Calcuttawala, R. T. Vest, D. Berdnik, N. Lu, O. Hahn, D. Gate, M. W. McNerney, D. Channappa, I. Cobos, N. Ludwig, W. J. Schulz-Schaeffer, A. Keller, T. Wyss-Coray, Dysregulation of brain and choroid plexus cell types in severe COVID-19. *Nature* **595**, 565–571 (2021).
4. C. Kaur, G. Rathnasamy, E.-A. Ling, The choroid plexus in healthy and diseased brain. *J. Neuropathol. Exp. Neurol.* **75**, 198–213 (2016).
5. V. Hubert, F. Chauveau, C. Dumot, E. Ong, L.-P. Berner, E. Canet-Soulas, J.-F. Ghersi-Egea, M. Wiart, Clinical imaging of choroid plexus in health and in brain disorders: A mini-review. *Front. Mol. Neurosci.* **12**, 34 (2019).

6. C. Johanson, E. Stopa, A. Baird, H. Sharma, Traumatic brain injury and recovery mechanisms: Peptide modulation of periventricular neurogenic regions by the choroid plexus–CSF nexus. *J. Neural Transm.* **118**, 115–133 (2011).
7. C. N. Bodnar, J. B. Watson, E. K. Higgins, N. Quan, A. D. Bachstetter, Inflammatory regulation of cns barriers after traumatic brain injury: A tale directed by interleukin-1. *Front. Immunol.* **12**, 688254 (2021).
8. M. C. Dewan, A. Rattani, S. Gupta, R. E. Baticulon, Y.-C. Hung, M. Punchak, A. Agrawal, A. O. Adeleye, M. G. Shrime, A. M. Rubiano, J. V. Rosenfeld, K. B. Park, Estimating the global incidence of traumatic brain injury. *J. Neurosurg.* **130**, 1080–1097 (2018).
9. Management of Concussion/mTBI Working Group, VA/DoD clinical practice guideline for management of concussion/mild traumatic brain injury. *J. Rehabil. Res. Dev.* **46**, CP1–CP68 (2009).
10. D. I. Katz, S. I. Cohen, M. P. Alexander, Mild traumatic brain injury. *Handb. Clin. Neurol.* **127**, 131–156 (2015).
11. S. C. Hellewell, C. S. Beaton, T. Welton, S. M. Grieve, Characterizing the risk of depression following mild traumatic brain injury: A meta-analysis of the literature comparing chronic mTBI to non-mTBI populations. *Front. Neurol.* **11**, 350 (2020).
12. D. E. Barnes, A. L. Byers, R. C. Gardner, K. H. Seal, W. J. Boscardin, K. Yaffe, Association of mild traumatic brain injury with and without loss of consciousness with dementia in US military veterans. *JAMA Neurol.* **75**, 1055–1061 (2018).
13. R. C. Gardner, A. L. Byers, D. E. Barnes, Y. Li, J. Boscardin, K. Yaffe, Mild TBI and risk of Parkinson disease: A chronic effects of neurotrauma consortium study. *Neurology* **90**, e1771–e1779 (2018).
14. W. Rutland-Brown, J. A. Langlois, L. Nicaj, R. G. Thomas Jr., S. A. Wilt, J. J. Bazarian, Traumatic brain injuries after mass-casualty incidents: Lessons from the 11 September 2001 World Trade Center attacks. *Prehosp. Disaster Med.* **22**, 157–164 (2007).
15. J. J. Kim, A. D. Gean, Imaging for the diagnosis and management of traumatic brain injury. *Neurotherapeutics* **8**, 39–53 (2011).
16. H. Zetterberg, D. H. Smith, K. Blennow, Biomarkers of mild traumatic brain injury in cerebrospinal fluid and blood. *Nat. Rev. Neurol.* **9**, 201–210 (2013).
17. A. Sharma, D. F. Muresanu, R. J. Castellani, A. Nozari, J. V. Lafuente, S. Sahib, Z. R. Tian, A. D. Buzoianu, R. Patnaik, L. Wiklund, H. S. Sharma, Mild traumatic brain injury exacerbates Parkinson's disease induced hemeoxygenase-2 expression and brain pathology: Neuroprotective effects of co-administration of TiO_2 nanowired mesenchymal stem cells and cerebrolysin. *Prog. Brain Res.* **258**, 157–231 (2020).
18. Z. Zhou, Z. R. Lu, Gadolinium-based contrast agents for magnetic resonance cancer imaging. *Wiley Interdiscip. Rev. Nanomed. Nanobiotechnol.* **5**, 1–18 (2013).
19. N. Iyad, M. S. Ahmad, S. G. Alkhatib, M. Hjouj, Gadolinium contrast agents-challenges and opportunities of a multidisciplinary approach: Literature review. *Eur. J. Radiol. Open* **11**, 100503 (2023).
20. J. Wahsner, E. M. Gale, A. Rodríguez-Rodríguez, P. Caravan, Chemistry of MRI contrast agents: Current challenges and new frontiers. *Chem. Rev.* **119**, 957–1057 (2018).
21. B.-Z. Qian, J. Li, H. Zhang, T. Kitamura, J. Zhang, L. R. Campion, E. A. Kaiser, L. A. Snyder, J. W. Pollard, CCL2 recruits inflammatory monocytes to facilitate breast-tumour metastasis. *Nature* **475**, 222–225 (2011).
22. A. Alam, E. P. Thelin, T. Tajsic, D. Z. Khan, A. Khellaf, R. Patani, A. Helmy, Cellular infiltration in traumatic brain injury. *J. Neuroinflammation* **17**, 328 (2020).
23. G. Huang, H. Huang, Application of hyaluronic acid as carriers in drug delivery. *Drug Deliv.* **25**, 766–772 (2018).
24. G. Stojkov, Z. Niyazov, F. Picchioni, R. K. Bose, Relationship between structure and rheology of hydrogels for various applications. *Gels* **7**, 255 (2021).
25. S. Gu, G. Cheng, T. Yang, X. Ren, G. Gao, Mechanical and rheological behavior of hybrid cross-linked polyacrylamide/cationic micelle hydrogels. *Macromol. Mater. Eng.* **302**, 1700402 (2017).
26. N. Doshi, A. J. Swiston, J. B. Gilbert, M. L. Alcaraz, R. E. Cohen, M. F. Rubner, S. Mitragotri, Cell-based drug delivery devices using phagocytosis-resistant backpacks. *Adv. Mater.* **23**, H105–H109 (2011).
27. T. J. Merkel, K. Chen, S. W. Jones, A. A. Pandya, S. Tian, M. E. Napier, W. E. Zamboni, J. M. DeSimone, The effect of particle size on the biodistribution of low-modulus hydrogel PRINT particles. *J. Control. Release* **162**, 37–44 (2012).
28. H. U. Kim, Y. H. Roh, S. J. Mun, K. W. Bong, Discontinuous dewetting in a degassed mold for fabrication of homogeneous polymeric microparticles. *ACS Appl. Mater. Interfaces* **12**, 53318–53327 (2020).
29. R. J. Jackman, D. C. Duffy, E. Ostuni, N. D. Willmore, G. M. Whitesides, Fabricating large arrays of microwells with arbitrary dimensions and filling them using discontinuous dewetting. *Anal. Chem.* **70**, 2280–2287 (1998).
30. N. Kapate, J. R. Clegg, S. Mitragotri, Non-spherical micro- and nanoparticles for drug delivery: Progress over 15 years. *Adv. Drug Deliv. Rev.* **177**, 113807 (2021).
31. Y. Xia, G. M. Whitesides, Soft lithography. *Angew. Chem. Int. Ed.* **37**, 550–575 (1998).
32. M. E. Helgeson, S. C. Chapin, P. S. Doyle, Hydrogel microparticles from lithographic processes: Novel materials for fundamental and applied colloid science. *Curr. Opin. Colloid Interface Sci.* **16**, 106–117 (2011).
33. J. Menges, P. Kleinschmidt, H.-J. Bart, E. Oesterschulze, A precision structured smart hydrogel for sensing applications. *J. Appl. Phys.* **122**, 134501 (2017).
34. S. Hassanpour-Tamrin, A. Sanati-Nezhad, A. Sen, A simple and low-cost approach for irreversible bonding of polymethylmethacrylate and polydimethylsiloxane at room temperature for high-pressure hybrid microfluidics. *Sci. Rep.* **11**, 4821 (2021).
35. S. D. Oberdick, G. Zabow, Patterned surface energy in elastomeric molds as a generalized approach to polymer particle fabrication. *ACS Appl. Polym. Mater.* **2**, 846–852 (2020).
36. T. Rutt, N. Eskandari, M. Zhurova, J. A. Elliott, L. E. McGann, J. P. Acker, J. A. Nychka, Thermal expansion of substrate may affect adhesion of Chinese hamster fibroblasts to surfaces during freezing. *Cryobiology* **86**, 134–139 (2019).
37. A. D. Elster, W. T. Sobol, W. H. Hinson, Pseudolayering of Gd-DTPA in the urinary bladder. *Radiology* **174**, 379–381 (1990).
38. G. E. Hagberg, K. Scheffler, Effect of r1 and r2 relaxivity of gadolinium-based contrast agents on the T1-weighted MR signal at increasing magnetic field strengths. *Contrast Media Mol. Imaging* **8**, 456–465 (2013).
39. J. S. Ananta, B. Godin, R. Sethi, L. Moriggi, X. Liu, R. E. Serda, R. Krishnamurthy, R. Muthupillai, R. D. Bolskar, L. Helm, M. Ferrari, L. J. Wilson, P. Decuzzi, Geometrical confinement of gadolinium-based contrast agents in nanoporous particles enhances T 1 contrast. *Nat. Nanotechnol.* **5**, 815–821 (2010).
40. V. Jacques, S. Dumas, W.-C. Sun, J. S. Troughton, M. T. Greenfield, P. Caravan, High-relaxivity magnetic resonance imaging contrast agents part 2: Optimization of inner-and second-sphere relaxivity. *Invest. Radiol.* **45**, 613–624 (2010).
41. S. Gyoneva, R. M. Ransohoff, Inflammatory reaction after traumatic brain injury: therapeutic potential of targeting cell–cell communication by chemokines. *Trends Pharmacol. Sci.* **36**, 471–480 (2015).
42. A. Z. Khawaja, D. B. Cassidy, J. Al Shakarchi, D. G. McGrogan, N. G. Inston, R. G. Jones, Revisiting the risks of MRI with Gadolinium based contrast agents—Review of literature and guidelines. *Insights Imaging* **6**, 553–558 (2015).
43. D. Hickman, J. Johnson, T. Vemulapalli, J. Crisler, R. Shepherd, Commonly used animal models. *Principles of Animal Res. for Graduate and Undergrad. Stud.*, 117–175 (2017).
44. S. K. Shin, E. E. Kaiser, F. D. West, Alcohol induced brain and liver damage: Advantages of a porcine alcohol use disorder model. *Front. Physiol.* **11**, 592950 (2021).
45. B. Thapa, A. Walia, Liver function tests and their interpretation. *The Indian J. of Pediatr.* **74**, 663–671 (2007).
46. V. Gounden, H. Bhatt, I. Jialal, Renal function tests. (2018).
47. R. Vink, Large animal models of traumatic brain injury. *J. Neurosci. Res.* **96**, 527–535 (2018).
48. S. Lee, S. Kivimäe, A. Dolor, F. C. Szoka, Macrophage-based cell therapies: The long and winding road. *J. Control. Release* **240**, 527–540 (2016).
49. P. A. Yushkevich, J. Piven, H. C. Hazlett, R. G. Smith, S. Ho, J. C. Gee, G. Gerig, User-guided 3D active contour segmentation of anatomical structures: Significantly improved efficiency and reliability. *Neuroimage* **31**, 1116–1128 (2006).
50. A. Fallacara, E. Baldini, S. Manfredini, S. Vertuani, Hyaluronic acid in the third millennium. *Polymers* **10**, 701 (2018).
51. H. Zhong, G. Chan, Y. Hu, H. Hu, D. Ouyang, A comprehensive map of FDA-approved pharmaceutical products. *Pharmaceutics* **10**, 263 (2018).
52. E. Uribe-Querol, C. Rosales, Phagocytosis: Our current understanding of a universal biological process. *Front. Immunol.* **11**, 1066 (2020).
53. Q. Taban, P. T. Mumtaz, K. Z. Masoodi, E. Haq, S. M. Ahmad, Scavenger receptors in host defense: from functional aspects to mode of action. *Cell Commun. Sig.* **20**, 1–17 (2022).
54. A. Palecanda, L. Kobzik, Receptors for unopsonized particles: the role of alveolar macrophage scavenger receptors. *Curr. Mol. Med.* **1**, 589–595 (2001).
55. J. A. Champion, S. Mitragotri, Role of target geometry in phagocytosis. *Proc. Natl. Acad. Sci.* **103**, 4930–4934 (2006).
56. S. Laus, A. Sour, R. Ruloff, E. Toth, A. E. Merbach, Rotational dynamics account for pH-dependent relaxivities of PAMAM dendrimeric, Gd-based potential MRI contrast *Agents*. *Eur. J.* **11**, 3064–3076 (2005).
57. C. Mondadori, M. Crippa, M. Moretti, C. Candrian, S. Lopa, C. Arrigoni, Advanced microfluidic models of cancer and immune cell extravasation: A systematic review of the literature. *Front. Bioeng. Biotechnol.* **8**, 907 (2020).
58. J. Qiao, S. Xue, F. Pu, N. White, J. Jiang, Z.-R. Liu, J. J. Yang, Molecular imaging of EGFR/HER2 cancer biomarkers by protein MRI contrast agents. *JBIC J. Biol. Inorg. Chem.* **19**, 259–270 (2014).
59. J. Davies, P. Siebenhandl-Wolff, F. Tranquart, P. Jones, P. Evans, Gadolinium: Pharmacokinetics and toxicity in humans and laboratory animals following contrast agent administration. *Arch. Toxicol.* **96**, 403–429 (2022).
60. K. J. Wolf, S. Kumar, Hyaluronic acid: Incorporating the bio into the material. *ACS Biomater Sci. Eng.* **5**, 3753–3765 (2019).
61. P. M. Kharkar, K. L. Kiick, A. M. Kloxin, Designing degradable hydrogels for orthogonal control of cell microenvironments. *Chem. Soc. Rev.* **42**, 7335–7372 (2013).
62. C. C. Schuurmans, A. J. Brouwer, J. A. Jong, G.-J. P. Boons, W. E. Hennink, T. Vermonden, Hydrolytic (In) stability of methacrylate esters in covalently cross-linked hydrogels based

on chondroitin sulfate and hyaluronic acid methacrylate. *ACS omega* **6**, 26302–26310 (2021).
63. M. Yokoyama, K. Shiraishi, Stability evaluation of Gd chelates for macromolecular MRI contrast agents. *Magnetic Reson. Mater. Phys Biol. Med.* **33**, 527–536 (2020).
64. M. Rogosnitzky, S. Branch, Gadolinium-based contrast agent toxicity: A review of known and proposed mechanisms. *Biometals* **29**, 365–376 (2016).
65. F. Amyot, D. B. Arciniegas, M. P. Brazaitis, K. C. Curley, R. Diaz-Arrastia, A. Gandjbakhche, P. Herscovitch, S. R. Hinds, G. T. Manley, A. Pacifico, A review of the effectiveness of neuroimaging modalities for the detection of traumatic brain injury. *J. Neurotrauma* **32**, 1693–1721 (2015).
66. B. Lee, A. Newberg, Neuroimaging in traumatic brain imaging. *NeuroRx* **2**, 372–383 (2005).
67. E. J. Meyer, J. N. Stout, A. W. Chung, P. E. Grant, R. Mannix, B. Gagoski, Longitudinal changes in magnetic resonance spectroscopy in pediatric concussion: A pilot study. *Front. Neurol.* **10**, 556 (2019).
68. T. A. Maugans, C. Farley, M. Altaye, J. Leach, K. M. Cecil, Pediatric sports-related concussion produces cerebral blood flow alterations. *Pediatrics* **129**, 28–37 (2012).
69. R. Mannix, N. J. Morriss, G. M. Conley, W. P. Meehan III, A. Nedder, J. Qiu, J. Float, C. A. DiCesare, G. D. Myer, Internal jugular vein compression collar mitigates histopathological alterations after closed head rotational head impact in swine: A pilot study. *Neuroscience* **437**, 132–144 (2020).
70. J. Szmydynger-Chodobska, N. Strazielle, J. R. Gandy, T. H. Keefe, B. J. Zink, J.-F. Ghersi-Egea, A. Chodobski, Posttraumatic invasion of monocytes across the blood—cerebrospinal fluid barrier. *J. Cereb. Blood Flow Metabol.* **32**, 93–104 (2012).
71. D. Demeestere, C. Libert, R. E. Vandenbroucke, Clinical implications of leukocyte infiltration at the choroid plexus in (neuro) inflammatory disorders. *Drug Discov. Today* **20**, 928–941 (2015).
72. R. B. Meeker, K. Williams, D. A. Killebrew, L. C. Hudson, Cell trafficking through the choroid plexus. *Cell Adh. Migr.* **6**, 390–396 (2012).
73. R. Shechter, A. London, M. Schwartz, Orchestrated leukocyte recruitment to immune-privileged sites: Absolute barriers versus educational gates. *Nat. Rev. Immunol.* **13**, 206–218 (2013).
74. M. Feng, Assessment of blood-brain barrier penetration: In silico, in vitro and in vivo. *Curr. Drug Metab.* **3**, 647–657 (2002).
75. P. Solár, A. Zamani, L. Kubíčková, P. Dubový, M. Joukal, Choroid plexus and the blood–cerebrospinal fluid barrier in disease. *Fluids Barr. CNS* **17**, 1–29 (2020).
76. J. Xia, Z. Wang, D. Huang, Y. Yan, Y. Li, J. Guan, Asymmetric biodegradable microdevices for cell-borne drug delivery. *ACS Appl. Mater. Interfaces* **7**, 6293–6299 (2015).
77. C. Wang, S. Wang, Y. Zhang, Z. Wang, J. Liu, M. Zhang, Self-polymerization and co-polymerization kinetics of gadolinium methacrylate. *J. Rare Earths* **36**, 298–303 (2018).
78. M. Guvendiren, J. A. Burdick, Stiffening hydrogels to probe short- and long-term cellular responses to dynamic mechanics. *Nat. Commun.* **3**, 1–9 (2012).
79. P. Zhang, J. Guan, Fabrication of multilayered microparticles by integrating layer-by-layer assembly and microcontact printing. *Small* **7**, 2998–3004 (2011).
80. D. Qin, Y. Xia, G. M. Whitesides, Soft lithography for micro- and nanoscale patterning. *Nat. Protoc.* **5**, 491–502 (2010).
81. V. S. Marangoni, O. Neumann, L. Henderson, C. C. Kaffes, H. Zhang, R. Zhang, S. Bishnoi, C. Ayala-Orozco, V. Zucolotto, J. A. Bankson, Enhancing T1magnetic resonance imaging contrast with internalized gadolinium(III) in a multilayer nanoparticle. *Proc. Natl. Acad. Sci.* **114**, 6960–6965 (2017).
82. X. Zhang, R. Goncalves, D. M. Mosser, The isolation and characterization of murine macrophages. *Curr. Protoc. Immunol.* **Chapter 14**, 1411 (2008).
83. M. A. Evans, P. J. Huang, Y. Iwamoto, K. N. Ibsen, E. M. Chan, Y. Hitomi, P. C. Ford, S. Mitragotri, Macrophage-mediated delivery of light activated nitric oxide prodrugs with spatial, temporal and concentration control. *Chem. Sci.* **9**, 3729–3741 (2018).
84. A. Fernandez, E. J. Thompson, J. W. Pollard, T. Kitamura, M. Vendrell, A Fluorescent activatable AND-gate chemokine CCL2 enables in vivo detection of metastasis-associated macrophages. *Angew. Chem. Int. Ed.* **58**, 16894–16898 (2019).
85. K. M. Guskiewicz, J. P. Mihalik, Biomechanics of sport concussion. *Exerc. Sport Sci. Rev.* **39**, 4–11 (2011).
86. P. Bankhead, M. B. Loughrey, J. A. Fernández, Y. Dombrowski, D. G. McArt, P. D. Dunne, S. McQuaid, R. T. Gray, L. J. Murray, H. G. Coleman, QuPath: Open source software for digital pathology image analysis. *Sci. Rep.* **7**, 1–7 (2017).
87. N. J. Morriss, G. M. Conley, S. M. Ospina, W. P. Meehan III, J. Qiu, R. Mannix, Automated quantification of immunohistochemical staining of large animal brain tissue using QuPath software. *Neuroscience* **429**, 235–244 (2020).

Acknowledgments: We thank O. Adebowale for assistance with material preparation. We also thank the Langmuir Group Department of Earth and Planetary Sciences at Harvard University for ICP-MS service, the Allston Science and Engineering Complex's Molecular and Cellular Biology Core and Harvard University Center for Nanoscale Systems (CNS), a member of the National Nanotechnology Coordinated Infrastructure Network (NNCI) supported by NSF ECCS-2025158. We also thank the Comparative Pathology and Genomics Shared Resource (CCPGSR) in the Cummings School of Veterinary Medicine at Tufts University, North Grafton, MA, for the service of histological tissue preparation. We acknowledge BioRender.com for schematic creation and Dragonfly software for advanced analysis and visualization of MRI images. S.M. acknowledges support from the John A. Paulson School of Engineering and Applied Sciences at Harvard University. **Funding:** This work was supported by the grant W81XWH-19-2-0011 from the Defense Medical Research and Development Program by the Department of Defense (to S.M. and R.M.), a NSF Graduate Research Fellowship grant no. 1122374 (to N. Kapate), and NSF Graduate Research Fellowship under grant no. 1745302 (to M.J.). **Author contributions:** L.L.-W.W. conceived, designed, and conducted the experiments, analyzed the data, and wrote and revised the paper. Y.G. contributed to the experimental design and data analysis of material synthesis and hydrogel characterization, providing critical discussions for important intellectual content. V.C.S. contributed to the data analysis of MRI images, material preparation, and provided critical revisions for important intellectual content. M.L.B. contributed to the experimental design, conducted the porcine studies, and edited the manuscript. S.S., N. Kapate, R.L., N. Kumbhojkar, S.P., M.J., and K.S.P. contributed to material preparation, provided intellectual discussion, and edited the manuscript. T.S. contributed to the in vitro MRI studies and manuscript editing. J.R.C. contributed to the experimental design of material synthesis and provided intellectual discussion. K.W. contributed to the logistics and conduction of the porcine studies. M.D., B.I., A.L., and S.D. contributed to material preparation and manuscript editing. C.J. contributed to the porcine MRI study design, intellectual discussion on MRI data analysis, and provided critical revisions for intellectual clinical content. R.M. sourced the funding, supervised the porcine studies, and provided critical revisions for intellectual clinical content. S.M. conceived the project, provided intellectual content, sourced the funding, supervised the overall project, provided guidance throughout the research process, and reviewed and revised the manuscript. **Competing interests:** L.L.-W.W., Y.G., N. Kapate, N. Kumbhojkar, S.P., and S.M. are inventors on patent applications related to the results described in the manuscript ("Compositions and methods relating to cells with adhered particles"; International Application No. PCT/US22/37261 and US Provisional Application No. 63/222,120 that are owned and managed by Harvard University). S.M. is a board member and shareholder of Hitch Bio. The other authors declare no competing interests. **Data and materials availability:** All data associated with this study are in the paper or the Supplementary Materials. The GLAMs generated in this study can be provided by contacting the corresponding author under a Harvard materials transfer agreement.

Submitted 1 September 2023
Accepted 29 November 2023
Published 3 January 2024
10.1126/scitranslmed.adk5413

Science Translational Medicine

Preclinical characterization of macrophage-adhering gadolinium micropatches for MRI contrast after traumatic brain injury in pigs

Lily Li-Wen Wang, Yongsheng Gao, Vineeth Chandran Suja, Masen L. Boucher, Suyog Shaha, Neha Kapate, Rick Liao, Tao Sun, Ninad Kumbhojkar, Supriya Prakash, John R. Clegg, Kaitlyn Warren, Morgan Janes, Kyung Soo Park, Michael Dunne, Bolu Ilelaboye, Andrew Lu, Solomina Darko, Camilo Jaimes, Rebekah Mannix, and Samir Mitragotri

Sci. Transl. Med. **16** (728), eadk5413. DOI: 10.1126/scitranslmed.adk5413

Editor's summary

Traumatic brain injury (TBI) elicits inflammatory responses, including the brain infiltration of macrophages through the choroid plexus. Wang and colleagues designed macrophage-adhering gadolinium-loaded anisotropic micropatches (GLAMs) to test whether tracking of macrophages tagged with GLAMs could improve MRI imaging after TBI. GLAMs had high contrast efficacy and adhered to macrophages without impeding their function. In vivo experiments in pigs showed that MRI of the choroid plexus using macrophages tagged with GLAMs allowed us to differentiate between sham- and TBI-exposed animals. Although more experiments are needed to validate these findings, GLAMs could help improve MRI for TBI. —Daniela Neuhofer

Science Translational Medicine (ISSN 1946-6242) is published by the American Association for the Advancement of Science. 1200 New York Avenue NW, Washington, DC 20005. The title *Science Translational Medicine* is a registered trademark of AAAS.